RESEARCH ARTICLE

SmartMat WILEY

Single atom and defect engineering of CuO for efficient electrochemical reduction of CO_2 to C_2H_4

Senlin Chu[1] | Changwoo Kang[2] | Woonghyeon Park[2] | Yu Han[1] |
Song Hong[1] | Leiduan Hao[1] | Hao Zhang[3] | Tsz Woon Benedict Lo[3] |
Alex W. Robertson[4] | Yousung Jung[2] | Buxing Han[5] | Zhenyu Sun[1] 🔵

[1]State Key Laboratory of Organic-Inorganic Composites, Beijing University of Chemical Technology, Beijing, China

[2]Department of Chemical and Biomolecular Engineering, Korea Advanced Institute of Science and Technology (KAIST), Daejeon, Republic of Korea

[3]Department of Applied Biology and Chemical Technology, The Hong Kong Polytechnic University, Hong Kong, China

[4]Department of Physics, University of Warwick, Coventry, UK

[5]Institute of Chemistry, Chinese Academy of Sciences, Beijing, China

Correspondence
Yousung Jung, Department of Chemical and Biomolecular Engineering, Korea Advanced Institute of Science and Technology (KAIST), Daejeon 34141, Republic of Korea.
Email: ysjn@kaist.ac.kr

Buxing Han, Institute of Chemistry, Chinese Academy of Sciences, Beijing 100190, China.
Email: hanbx@iccas.ac.cn

Zhenyu Sun, State Key Laboratory of Organic-Inorganic Composites, Beijing University of Chemical Technology, Beijing 100029, China.
Email: sunzy@mail.buct.edu.cn

Abstract

Electrochemical CO_2 transformation to high-value ethylene (C_2H_4) at high currents and efficiencies is desired and yet remains a grand challenge. We show for the first time that coupling single Sb atoms and oxygen vacancies of CuO enable synergistic electrocatalytic reduction of CO_2 to C_2H_4 at low overpotentials. Highly dispersed Sb atoms occupying metal substitutional sites of CuO are synthesized under mild conditions. The overall CO_2 reduction faradaic efficiency (FE) reaches $89.3 \pm 1.1\%$ with an FE toward C_2H_4 exceeding 58.4% at a high-current density of 500 mA/cm². Addition of the p-block metal is found to induce transformation of CuO from flakes to nanoribbons rich in nanoholes and oxygen vacancies, greatly enhancing CO_2 adsorption and activation while suppressing hydrogen evolution. Further density functional theory calculations with in situ X-ray diffraction reveal that combining Sb sites and oxygen vacancies prominently lessen the dimerization energy of adsorbed CO intermediate, thus boosting the conversion of CO_2 to produce C_2H_4. This study provides a new perspective for promoting selective C–C coupling for electrochemical CO_2 reduction.

KEYWORDS
CO_2 reduction, copper oxide, electrocatalysis, ethylene, single sites

1 | INTRODUCTION

The atmospheric concentration of CO_2 has increased dramatically from its preindustrial level of 285 ppm (parts per million) around 1850 to ~415.5 ppm in June 2021, leading to an unprecedented anthropogenic greenhouse effect.[1,2] As a result, the global average surface temperature has risen by about 1.2°C. In this context, electrochemical CO_2 reduction (ECR) using renewable electricity offers an appealing strategy for organic synthesis, allowing for sustainable and low carbon-footprint chemistry and also circumventing the requirement for sophisticated and energy-intense plant designs.[3–5] Relative to C_1 compounds, ECR to multicarbon chemicals is more attractive owing to their higher energy density, market value, and broader applications.[6–8] Among different products, ethylene (C_2H_4) is highly desired as an industrial feedstock for polyethylene production. Nevertheless, electro-conversion of CO_2 to C_2H_4 is challenging because of the slow C–C coupling kinetics, high C–C coupling energy penalty, and competition between C–C, C–O, and C–H bond formation.[9] In addition, multielectron transfer processes (12 electrons) are required to generate C_2H_4. Among others, the parasitic hydrogen evolution reaction (HER) always takes place in water-based electrolytes under similar potentials.[10]

An adsorbed CO_2 molecule is first reduced to a carboxyl intermediate *COOH via a concerted proton–electron transfer process, and then to *CO (*represents surface adsorbed species) and a water molecule. *CO is recognized to be a common intermediate for the production of C_2H_4. Three major schemes have been proposed for C_2H_4 evolution: (1) "carbene" pathway; (2) dimerization of two *CO species; and (3) reaction of CHO* with *CO or CHO*.[11] In the carbene mechanism, hydroxycarbene or atomic carbon is formed which is further converted to *CH₂. Subsequent combination of two *CH₂ adsorbates or insertion of CO in *CH₂ results in C_2H_4. Alternatively, dimerization of two *CO to yield C_2H_4 may occur especially at low overpotentials.[12] Specifically, *CO couples to form *C_2O_2 which is then hydrated to *OC–COH (via the EleyeRideal [ER] mechanism). C_2H_4 is generated from the transformation of the subsequent *CH₂–CHO intermediate. Besides, *OC–COH can be reduced to *COH=COH in the presence of adsorbed H_2O. Dihydroxylation of *COH=COH leads to the yield of *C=COH which is further transformed to *C=CH (via adsorbed H_2O or through the Langmuir–Hinshelwood [LH] mechanism). C_2H_4 can be obtained after cascade reductions (*C=CH₂ → *CH=CH₂ → *CHCH₃ → *CH₂CH₃) followed by β-elimination. At high overpotentials, *CO may be first reduced to *CHO and OC–CHO coupling is more kinetically favorable than *CO dimerization and reduction.[12] C_2H_4 is then produced through the subsequent formation and reduction of *OC–CHOH. An alternative path is CHO* + CHO* → OHC–CHO* → *H₂C–CHO → H₂C–CH₂O*. Direct cleavage of C–O bond in H₂C–CH₂O* or through hydrogenation to H₃C–CH₂OH* gives rise to C_2H_4.

Regardless of distinct pathways, the adsorbed *CO species has been recognized as a key intermediate for C–C bond formation to generate C_2H_4 and other C_{2+} products.[9,11,12] Hence, optimizing the population and binding of the *CO intermediate and concurrently reducing the relative ratio of adsorbed H (to impede the undesired HER) are necessary to accelerate the ECR to C_2H_4. To achieve this purpose, previous works have been devoted to the modification of Cu catalysts by heteroatom doping,[13,14] alloying,[15] morphology and facet control,[16,17] mixed oxidation states,[18] and interface engineering.[19,20] However, the C_2H_4 production efficiency remains insufficient, mostly due to the large C–C coupling barriers. To overcome this issue, the design and development of a synergistic catalytic system that enables enhancement of both CO_2 activation and C–C coupling offer a promising avenue. Here we report such a cooperative strategy by rationally tailoring the defects of CuO (e.g., oxygen vacancies (V_O) to boost CO_2 adsorption and activation) and also incorporating a second Sb single site (to increase *CO coverage for cascade reactions and also lower the free energy of C–C coupling). It remarkably promoted the C_2H_4 production, with a stable FE exceeding 46% at a mild overpotential regardless of prolonged electrolysis in an H-type electrochemical cell, substantially outweighing bare CuO(V_O) and many recently reported electrocatalysts. More importantly, the overall FE for ECR and the FE for C_2H_4 can be further improved up to 89.3% and 58.4%, respectively, with a high-current density of 500 mA/cm² in a flow reactor. In situ X-ray diffraction (XRD), X-ray absorption spectroscopy (XAS), and aberration-corrected high-angle annular dark-field scanning transmission electron microscopy (HAADF-STEM) analyses in conjunction with density functional theory (DFT) calculations were further performed to correlate the activity and product selectivity with structural characteristics of the catalytic systems, gaining fresh insights into the role of Sb atoms in promoting C–C coupling on multicrystalline CuO.
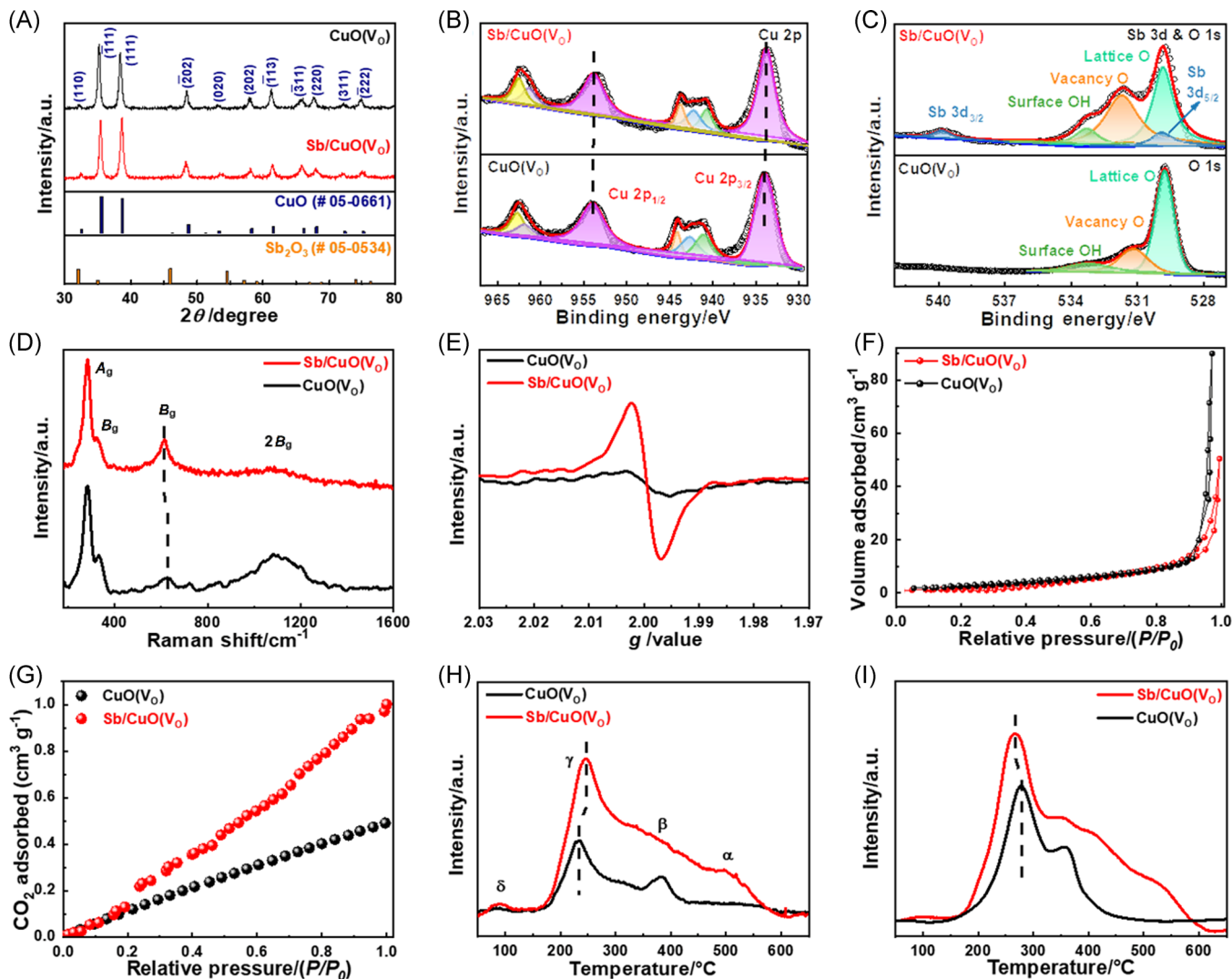
FIGURE 1 (A) X-ray diffraction patterns, (B) Cu 2p and (C) Sb 3d and O 1s core-level X-ray photoelectron spectroscopy spectra, (D) Raman spectra, (E) electron paramagnetic resonance spectra, (F) N_2 adsorption/desorption isotherms, (G) CO_2 adsorption isotherms, (H) CO_2, and (I) CO temperature-programmed desorption curves of the as-made $CuO(V_O)$ and $Sb/CuO(V_O)$

2 | RESULTS AND DISCUSSION

2.1 | Morphological and structural analyses

Single Sb atom modified CuO rich in defects (Sb/CuO (V_O)) were facilely fabricated for the first time by applying a straightforward wet chemical synthesis method without high-temperature treatments. No capping ligands are needed during the synthesis, ensuring clean surfaces for the samples and circumventing adverse effect from the stabilizer molecules. Figure 1A is the XRD patterns of pristine $CuO(V_O)$ and $Sb/CuO(V_O)$. Typical diffraction peaks appearing at about 32.2°, 35.2°, 38.5°, 48.6°, 53.3°, 58.0°, 61.3°, 65.9°, 67.8°, 72.2°, and 75° were

clearly observed for both samples, which can be well assigned to the (110), ($\bar{1}$11), (111), ($\bar{2}$02), (020), (202), ($\bar{1}$13), ($\bar{3}$11), (220), (311), ($\bar{2}$22) facets of monoclinic CuO, which is in line with the Joint Committee on Powder Diffraction Standards file (JCPDS No. 05-0661). No spectral features of Cu, Cu_2O, Sb, Sb_2O_3, and Sb_2O_5 were discernable, ruling out the formation of corresponding big crystals. It indicates that the Sb species present during synthesis did not coalesce into crystallinities detectable by XRD, and thus suggests the Sb species instead formed atomically dispersed Sb ions that integrated in CuO structure, which is confirmed by the following HAADF-STEM analysis. Note that a slight shift toward higher angles occurred with the increase of Sb content likely due to the ionic radii difference of Sb

(0.76 Å) and Cu (0.73 Å). The XRD peaks also became broader, potentially due to the lattice strain in CuO induced by Sb insertion.[21]

X-ray photoelectron spectroscopy (XPS) was employed to analyze the surface composition and chemical state of Sb/CuO(V_O) as well as any possible interaction between Sb and Cu. The wide-scan XPS spectrum discloses the spectroscopic characters of Cu, O, and Sb. No other elements (such as Cl) were detected, excluding the presence of impurities, remaining precursor or byproducts in the sample. A pronounced spin-orbit split doublet with Cu $2p_{1/2}$ at 954 eV and $2p_{3/2}$ at 934 eV was observed for CuO (Figure 1B), denoting the main valence state of Cu^{2+}. Three typical Cu^{2+} satellites at 962.6, 944, and 941.6 eV were also seen.[18,22] Relative to CuO(V_O), the Cu 2p electron binding energies in Sb/CuO(V_O) shifted to lower values. This can be ascribed to the compressive strain-induced electronic structure change of CuO triggered by the lattice constant mismatch of the interface between Sb and CuO. No obvious Cu^+ signal, expected around 951.9 (Cu $2p_{1/2}$) and 932.2 eV (Cu $2p_{3/2}$), was discernible. Two prominent bands at ~539.8 and ~530.4 eV manifested in Figure 1C are assigned to corresponding Sb $3d_{3/2}$ and Sb $3d_{5/2}$ peaks of Sb^{3+}.[23] Deconvolution of the O 1s spectra gives three sub-bands (Figure 1C). The weak peak at about 533.3 eV originates from the surface hydroxyl groups, whereas the other two oxygen peaks at ~531.2 and 530 eV are attributed to the vacancy oxygen and lattice oxygen, respectively.[24] Strikingly, the ratio of vacancy oxygen to lattice oxygen in Sb/CuO(V_O) was derived to be ~0.94, nearly threefold that of CuO (0.34). A high density of oxygen vacancies can significantly enhance the adsorption and activation of CO_2, thus facilitating its further conversion.

The local atomic arrangements and vibrations of Sb/CuO(V_O) were probed by Raman spectroscopy. Three appreciable one-phonon vibrations at ~286.6, 335.2, and 611 cm^{-1} shown in Figure 1D correspond to the single A_g mode and two B_g optical modes of CuO.[21] The Raman band of Sb/CuO(V_O) at 611 cm^{-1} is more intense and red-shifted as opposed to CuO, possibly owing to the formation of more CuO lattice defects. The peak at 1090.1 cm^{-1} could be ascribed to multiphonon transition (as a result of phonon anharmonic coupling in polar solids), which became dramatically broadened after the incorporation of Sb. This may arise from higher local numbers of anisotropic carriers in Sb/CuO(V_O), resulting in an enhancement in electronic movement along the x–y plane during photoexcitation or phonon–plasmon coupling.[25] No noticeable peaks attributed to Sb_2O_3 or Sb_2O_5 were identified, in accord with the aforementioned XRD results.

Electron paramagnetic resonance (EPR) spectra display weak signals for pure CuO (Figure 1E), indicating a low level of defects. In sharp contrast, Sb/CuO(V_O) exhibits a symmetric pair of strong peaks with the signal at $g \approx 2.00$, associated with trapped unpaired electrons by oxygen vacancies through adsorbed oxygen species from air,[26] in agreement with the XPS observations. These unpaired electrons tend to delocalize the lattice of CuO, favoring electron transfer to adsorbates during the ECR process.

Figure 1F provides N_2 adsorption/desorption isotherms of CuO(V_O) and Sb/CuO(V_O). Both samples show a characteristic type H3 of the III isotherm based on the Brunauer–Deming–Deming–Teller classification.[27] The Brunauer–Emmett–Teller specific surface area and single-point total pore volume of Sb/CuO(V_O) were determined to be ~6.7 m^2/g and 0.06 cm^3/g respectively, relatively lower than 8.3 m^2/g and 0.14 cm^3/g for CuO (V_O). It suggests that the enhancement of CO_2 electrocatalysis on Sb/CuO(V_O) unlikely resulted from increased surface areas.

Intriguingly, Sb/CuO(V_O) possesses a substantially higher capacity of CO_2 uptake than CuO(V_O) (Figure 1G). This unambiguously favors the enriched concentration of CO_2 on the surface of Sb/CuO (V_O), hence boosting reaction kinetics. Further CO_2 temperature-programmed desorption (TPD) revealed that Sb/CuO(V_O) exhibits much stronger chemisorption of CO_2 in a wide temperature range (~180–580°C) compared to CuO(V_O), potentially providing benefits for ECR. The enhanced CO_2 adsorption may be the result of increased electron density at the catalyst surface due to electron transfer from Sb to Cu, leading to a larger charge transfer from substrate to CO_2.

Adsorbed CO* has been recognized as a key intermediate for ECR to form C_2H_4 and other multicarbon products. Therefore, the adsorption behavior of CO on the catalyst was examined by TPD of CO (CO-TPD). CO desorption took place at temperatures exceeding 260°C for both CuO(V_O) and Sb/CuO(V_O) (Figure 1I), suggesting the strong binding energies of CO in both cases. Sb/CuO(V_O) exhibited comparatively lower CO desorption temperature relative to bare CuO(V_O), alleviating poisoning of active sites due to too strong *CO binding energy. Especially, Sb/CuO(V_O) was observed to possess higher amounts of CO desorption than CuO(V_O). This plausibly boosts *CO coverage and subsequent dimerization.

Synchrotron radiation X-ray absorption fine structure (XAFS) was further used to detect the local atomic order and valence state of Sb and Cu in Sb/CuO(V_O). Figure 2A presents the Sb K-edge soft X-ray absorption near-edge structure (XANES) spectra of Sb/CuO(V_O) alongside
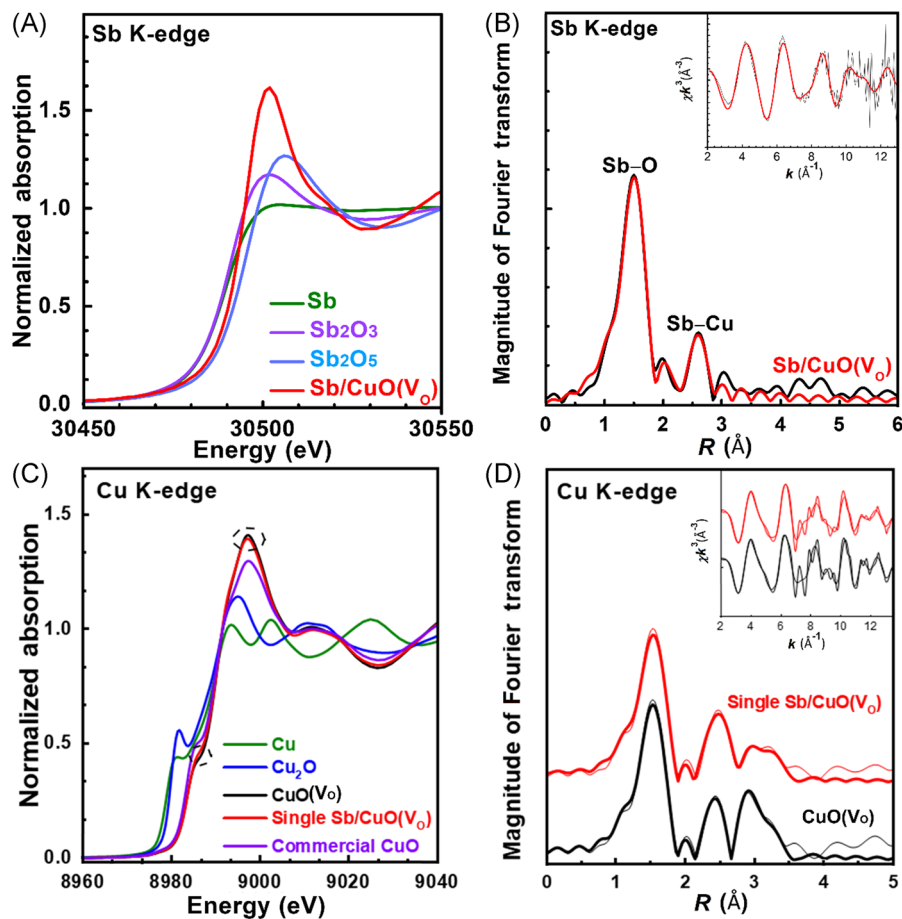
FIGURE 2 (A) Sb K-edge X-ray absorption near-edge structure spectra of Sb/CuO(V_O) along with those of Sb foil, Sb_2O_3, and Sb_2O_5 as reference standards. (B) Fourier-transformed Sb K-edge extended X-ray absorption fine structure (EXAFS) spectrum of Sb/CuO(V_O) at the Sb K-edge. (C) Cu K-edge XANES spectra of CuO(V_O) and Sb/CuO(V_O) as well as Cu foil, Cu_2O, and commercial CuO. (D) Fourier-transformed EXAFS spectra of CuO(V_O) and Sb/CuO(V_O) at the Cu K-edge

Sb_2O_5, Sb_2O_3, and Sb foil. The line intensity for Sb/CuO(V_O) was found to be remarkably higher than those of Sb_2O_5, Sb_2O_3, and Sb foil. By comparison with the reference samples according to whiteline peak position, the Sb atoms in Sb/CuO(V_O) are predominantly in +3 state. The Sb K-edge extended XAFS (EXAFS) curve was acquired by Fourier transforming the XAFS oscillations ($k^3x(k)$) (Figure 2B). The bond type, distance, and R-factor between an Sb atom and its nearest neighbor were estimated and included in Table S1. In addition to a small peak arising from Sb–Cu, a dominant peak at 1.48 Å was observed, which can be attributed to the Sb–O bond. It indicates that Sb atoms are prone to occupy metal substitutional sites of CuO. The number of oxygen situated around Sb was estimated to be 5.7, less than that of CuO (6). This signifies that oxygen vacancies were introduced adjacent to Sb atoms and/or some Sb atoms were located on the surface or in the subsurface of the cupric oxide. The Cu K-edge XANES spectra of the as-obtained CuO and Sb/CuO(V_O) together with commercial CuO, Cu_2O, and Cu foil are depicted in Figure 2C. The Cu in Sb/CuO(V_O) exhibits a lower edge position and line intensity, an indication of being partly reduced upon the incorporation of Sb. Fourier transformed EXAFS (Figure 2D) manifested a smaller coordination

number of oxygen for Cu in Sb/CuO(V_O) compared to bare CuO, illustrating the creation of more oxygen vacancies in the composite system.

Morphological and structural characterization by scanning electron microscopy (SEM) (Figure S1) and HAADF-STEM (Figure 3) showed the transformation of thick flakes of CuO (that randomly stack on top of each other) to a star-like assembly of thin nanoribbons after the decoration of Sb. This greatly increases the exposure of edges and surface active sites. Most nanoribbons were observed to curl up (Figure 3A). HAADF-STEM imaging (Figure 3B,C) along with simultaneous energy-dispersive X-ray (EDX) elemental maps (Figure 3D–F) indicated the prevalence and homogeneous distributions of Sb, Cu, and O across the sample. Several irregular holes that are less than 5 nm in diameter are distributed on the surface (especially at the thinner edges) of Sb/CuO(V_O), as vividly seen in Figure 3G. Interestingly, a number of bright spots were found to be well dispersed on the surface of crystalline CuO (Figure 3H–N). These spots can be reasonably assigned to single Sb atoms given the significantly larger atomic number of Sb compared to Cu or O will translate into a brighter appearance in HAADF-STEM. Enlarged HAADF-STEM images further validate the formation of singly separated Sb atoms
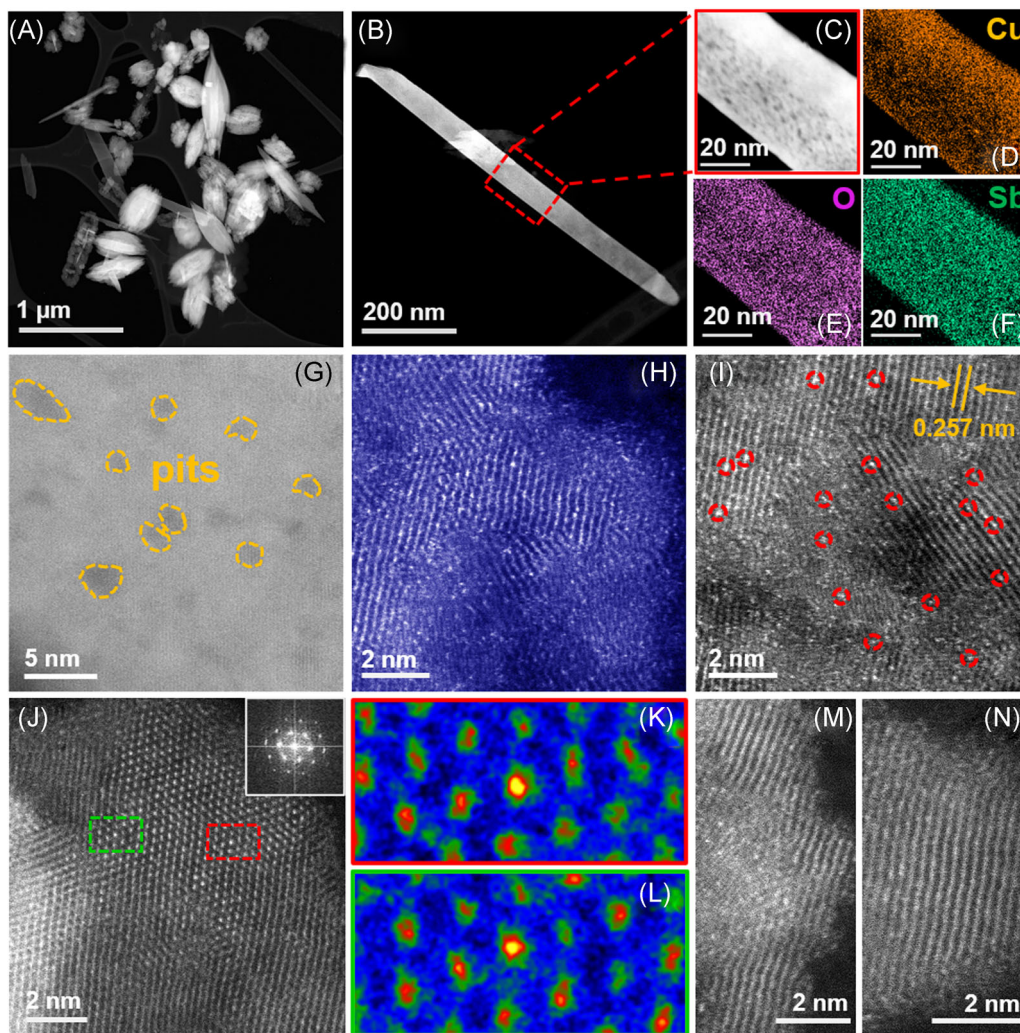
FIGURE 3 (A) Low-magnification and (B) high-magnification scanning transmission electron microscopy (STEM) images of Sb/CuO (V_O). (C) Enlarged high-angle annular dark-field (HAADF)-STEM image of the area encased by the red dashed rectangle in (B) and corresponding energy-dispersive X-ray maps of (D) Cu, (E) O, and (F) Sb of Sb/CuO(V_O). (G–J) HAADF-STEM images of Sb/CuO(V_O). In image (I), some individual Sb atoms are marked with red dashed circles to guide the eyes. The inset in (J) is its fast Fourier transform (FFT) pattern. (K) and (L) show transformed STEM images of the regions encased in red and green rectangles in (J), respectively. (M) and (N) HAADF-STEM images of Sb/CuO(V_O)

(Figure 3K,L). CuO was observed to be highly crystalline displaying clear interference fringes with a *d*-spacing of ca. 0.257 nm corresponding to the ($\bar{1}$ 11) plane (Figure 3I). Additionally, lattice deformation of CuO was observed for many of the nanoribbons, which may be caused by the incorporation of Sb atoms (Figure 3M,N).

2.2 | Electrocatalytic property for CO_2 reduction

To evaluate the intrinsic catalytic properties of the samples, we first conducted the ECR in CO_2-saturated 0.1 mol/L $KHCO_3$ aqueous electrolyte (pH 6.8) using an H-cell with continuous CO_2 flow.[20] All potentials mentioned are

hereafter with respect to reversible hydrogen electrode. The potential-dependent geometric current densities of Sb/CuO (V_O) and bare CuO(V_O) were recorded by linear sweep voltammetry (LSV). Dramatically larger reduction currents were attained in a CO_2 environment than in an Ar environment within the potential region from 0 to −1.4 V (Figure 4A). Strikingly, the incorporation of single Sb atoms on the surface of CuO could effectively hamper hydrogen evolution and greatly facilitate CO_2 reduction (Figure S2). The FE and yield rate of each reduction product were determined according to gas chromatography and proton nuclear magnetic resonance measurements.[20] CO, HCOOH, and C_2H_4 were found to be the major reduction products within the switching voltages from −0.75 to −1.2 V (Figure 4B). Conversion of CO_2 to C_2H_4 was found
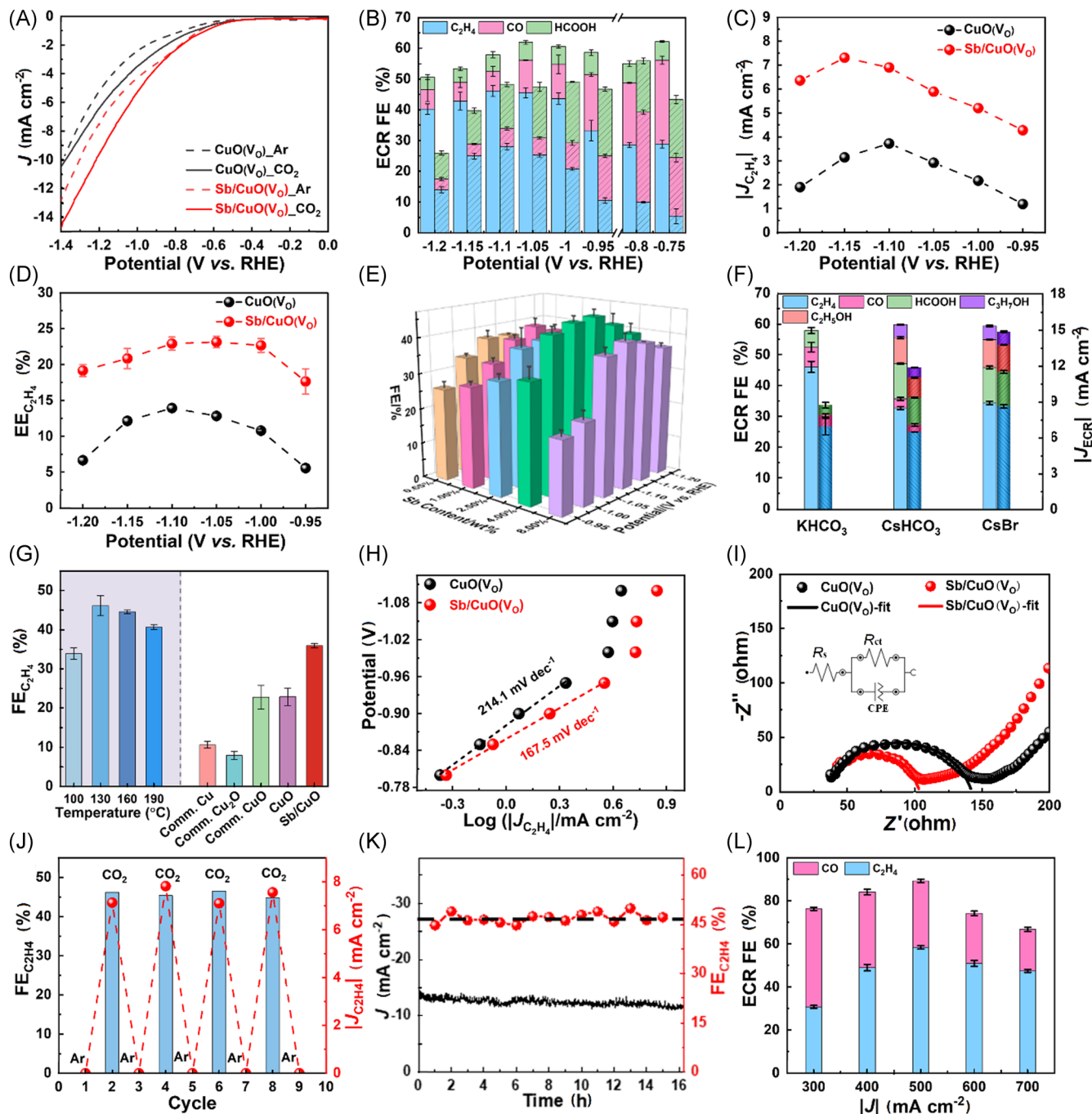
FIGURE 4 (A) Linear sweep voltammetry curves of CuO(V$_O$) and Sb/CuO(V$_O$) in 0.1 mol/L KHCO$_3$ purged with Ar or CO$_2$. (B) Electrochemical CO$_2$ reduction (ECR) faradaic efficiency (FE) and (C) partial C$_2$H$_4$ geometric current density, and (D) C$_2$H$_4$ cathodic energy efficiency (EE) over CuO(V$_O$) and Sb/CuO(V$_O$) against switching bias. (E) C$_2$H$_4$ FE as a function of Sb content at distinct measured voltages. (F) ECR FE and current density (J_{ECR}, grid columns) on Sb/CuO(V$_O$) in different electrolytes with concentration of 0.1 mol/L at −1.1 V. (G) C$_2$H$_4$ FEs over commercial Cu powder (Comm. Cu), commercial Cu$_2$O (Comm. Cu$_2$O), commercial CuO (Comm. CuO), Sb/CuO, and Sb/CuO(V$_O$) acquired at varying synthesis temperatures at −1.1 V. (H) Tafel plots of the partial C$_2$H$_4$ geometric current density and (I) Nyquist curves with corresponding fitting profiles for CuO(V$_O$) and Sb/CuO(V$_O$). The inset gives the equivalent circuit used for fitting the data, where R_S represents the combination of the resistance of electrodes and electrolyte, CPE and R_{ct} correspond to the capacitance and charge transfer resistance of working electrode–electrolyte interface. (J) C$_2$H$_4$ FE (blue columns) and partial C$_2$H$_4$ geometric current density (red balls) on Sb/CuO(V$_O$) during cycling electrolysis with an interval of 1 h in CO$_2$-and Ar-purged 0.1 mol/L KHCO$_3$ at −1.1 V. (K) Geometric current density (bottom line) and C$_2$H$_4$ FE (top ball line) on Sb/CuO(V$_O$) as a function of CO$_2$ electrolysis time at −1.1 V. (L) FEs for ECR products at different applied current densities over single Sb/CuO(V$_O$) in 1 mol/L KOH electrolytes using a flow cell. Data in (B, D, E–G, J, L) are presented as average values ± standard errors obtained from the experimental results of three times

to take place at a low overpotential ≤821 mV (given the equilibrium thermodynamic potential for CO_2 reduction to C_2H_4 is 0.071 V vs. normal hydrogen electrode under 298.15 K and 1 atm). C_2H_4 comprises the predominant ECR product at potentials more negative than −0.8 V. Especially, the C_2H_4 FE on Sb/CuO(V_O) exceeds >40% in a wide potential range from −1.0 to −1.2 V, much higher than that of CuO(V_O) (Figure 4B). Both total ECR FE and the FE for C_2H_4 production steadily increased at potentials ranging from −0.75 to −1.05 V, but descended when further raising the overpotential plausibly due to the more severe competition from the HER. Throughout the potential window, Sb/CuO(V_O) distinctly outperforms CuO(V_O) in terms of ECR reaction rate, overall ECR FE, and C_2H_4 selectivity. An average maximum C_2H_4 FE of 46.2% was achieved at an electrode potential of −1.1 V on Sb/CuO (V_O), in stark contrast to 28% over pure CuO(V_O). Alternatively, the partial current density (Figure 4C) toward C_2H_4 on Sb/CuO(V_O) reached ~7.8 ± 0.4 mA/cm^2 at −1.15 V, 2.3 times that of CuO(V_O). Likewise, the cathodic C_2H_4 energy efficiency (EE) approached 23 ± 0.9% at ~15.2 mA/cm^2 (Figure 4D). Markedly, the FE of C_2H_4 and cathodic C_2H_4 EE surpass many recently reported Cu-based electrocatalysts, as summarized in Table S3. The ECR activity was tunable by regulating the content of Sb and electrolyte type. The optimal Sb content based on C_2H_4 FE (Figure 4E) was found to be 4 wt%. Excessive Sb loading may cause aggregation and formation of Sb_2O_3 nanoparticles, which is not conducive toward CO_2 reduction for C_2H_4 production. 0.1 mol/L $KHCO_3$ was observed to be superior to other individual and mixed electrolytes for ECR to yield C_2H_4 at −1.1 V (Figures 4F and S3). Whereas 0.1 mol/L CsBr was found to favor the preferential ECR to C_{2+} products with a corresponding FE of nearly 47.9% and an unprecedented partial current density as high as ~12 mA/cm^2 (Figure 4F). Under equivalent electrochemical conditions, it is noteworthy that Sb/CuO(V_O) considerably outperformed commercial Cu powder ($FE_{C_2H_4} = 10.6\%$), Cu_2O ($FE_{C_2H_4} = 7.9\%$), and commercial CuO ($FE_{C_2H_4} = 23.8\%$) (Figure 4G). Sb/CuO in the absence of V_O was also prepared, which however displayed appreciably lower ECR activity ($FE_{C_2H_4} = 35.9\%$ at −1.1 V) compared to Sb/CuO(V_O) (Figure 4G). This underlines the collaborative effect of single Sb sites and oxygen vacancies in promoting the selective conversion of CO_2.

To understand the superior activity of Sb/CuO(V_O), the Tafel plot and electrochemical impedance were examined. The Tafel slope was ~167.5 mV/dec for Sb/CuO(V_O), much lower than that of CuO(V_O) (~214.1 mV/dec) (Figure 4H). This insinuates that Sb/CuO(V_O) has comparatively more rapid kinetics for CO_2 reduction. The formation of the *CO intermediate for tandem catalysis on the surface of the catalysts may determine the reaction rate. Nyquist plots

(Figure 4I) manifested a significantly smaller charge transport resistance (R_{ct}) for Sb/CuO(V_O) than that for CuO(V_O), facilitating interfacial charge exchange between electrode and electrolyte.

Cycling experiments by alternated electrolysis between Ar- and CO_2-purged electrolytes showed that the C_2H_4 production remained constant for at least four cycles (Figure 4J). The absence of C_2H_4 in an Ar environment suggests that the supplied CO_2 is the primary source of carbon in the generated C_2H_4. Notably, no appreciable loss in C_2H_4 FE and current density occurred even after continued electrolysis for 16 h, indicating the excellent catalytic stability of Sb/CuO(V_O) (Figure 4K).

To circumvent the poor solubility and diffusion of CO_2 in aqueous solutions, we conducted further electrochemical measurements in a flow cell to shorten the diffusion path for the ECR. Large cathodic current densities of over 100 mA/cm^2 were easily attained in a flow reactor with 1 mol/L aqueous KOH. Actually, the total ECR FE over Sb/CuO(V_O) is higher than 66% throughout a wide current density range from 300 to 700 mA/cm^2, reaching 89.3 ± 1.1% at 500 mA/cm^2 (Figure 4L). Particularly, at such high-current density, an impressive FE of 58.4 ± 0.6% for C_2H_4 generation was achieved.

The evolution of the catalysts during the ECR was monitored by in situ XRD analysis (Figure 5). It can be seen that the Cu^{2+} in Sb/CuO(V_O) was rapidly reduced to Cu^0 and minor Cu^+ after 4 min of electrolysis at −1.1 V, while only after 15 min of operation can the reduction of Cu^{2+} (to both Cu^+ and Cu^0) take place over a bare CuO electrode. This observation suggests that Cu^+ is unlikely to contribute to the boosted ECR to C_2H_4 and the major active site is Cu^0 for the Sb/CuO (V_O) system.

From the in situ contour plot, the gradual disappearance of the CuO phase is apparent. The Bragg's peaks corresponding to the *C2/c* CuO phase completely vanished after 4 min on-stream. By the quantitative analysis of the XRD patterns (Table S4), we obtained the volume-weighted mean column heights (LVol) which are calculated using FWHMs and integral breadths (IBs) assuming intermediate crystallite size broadening modeled by Voigt function. Similarly, the microstrain, e_0 (dislocations, vacancies, and other defects) was calculated from FWHMs. We found the asymmetry parameter of CuO (a measure by the simple axial model) remains relatively unchanged during the disappearing process while the Bragg's peaks broadened (a measure of LVol), which indicates a homogeneous reduction process. The formation of *Pn-3m* Cu_2O phase has been noticed between 4 and 5 min on-stream. After 5 min, Cu_2O is completely disappeared. Meanwhile, we noted the gradual formation of the *Fm-3m* Cu phase from 4 min and the
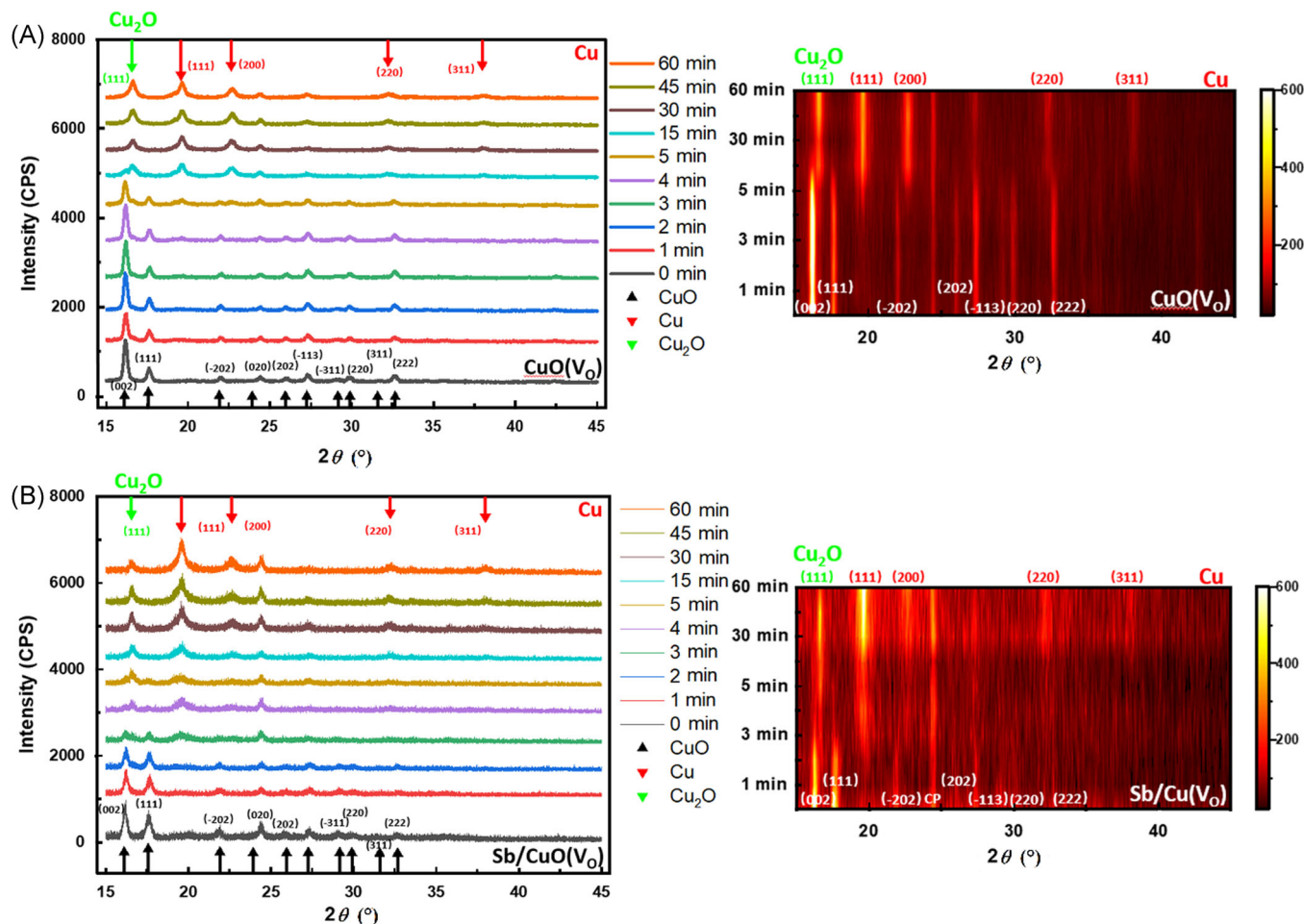
FIGURE 5 In situ X-ray diffraction profiles of (A) $CuO(V_O)$ and (B) $Sb/CuO(V_O)$ at -1.1 V for different time frames of CO_2 electrolysis

Bragg's peaks become more intense over time. From the quantitative analysis, the asymmetry parameters remain almost unchanged while the LVol parameters (based on the analysis of FWHMs and IBs) increase. Whereas peak asymmetry can be attributed to the inhomogeneous formation of Cu particles, and the increase in the LVol suggests the formation of larger nanoparticles.

2.3 | Theoretical calculations

We carried out DFT calculations to investigate the role of Sb for enhanced C_2 production on $Sb/CuO(V_O)$. Based on the experimental morphology characterization of $Sb/CuO(V_O)$ in the XRD results (Figure 1A), we considered a monoclinic-$CuO(V_O)(111)$ facet (Figure 6A). The $Sb/CuO(V_O)$ was then modeled by replacing one Cu atom with an Sb atom (Figure 6B). The positions of the Sb atom and the oxygen vacancy were determined according to a previous study.[28] As shown in Figure 4, C_2H_4 is the main product of CuO, and hence, we

considered the C_2H_4 production reaction pathway on both $CuO(V_O)$ and $Sb/CuO(V_O)$. We followed a previous mechanism of CO_2 reduction to C_2H_4 mechanism on the Cu surface (see Supporting Information).[29,30] All optimized structures of reaction intermediates are presented in Figures S4–S6.

The relative free energies along with the reaction mechanism are displayed in Figure 6C,D. First, we compared the reaction free energies of CO_2 to C_2H_4 on $CuO(V_O)$ and $Sb/CuO(V_O)$ (Figure 6D) to estimate the thermodynamic energy barrier. The overall energy schemes on both surfaces are similar and the potential determining step (PDS) is found to be the same with and without Sb incorporation, namely, the *COOH formation step $(* + CO_2 + (H^+ + e^-) \rightarrow *COOH)$ (0.98 eV). This result suggests that the thermodynamic stability of intermediates alone cannot explain the favorable C_2H_4 production on the $Sb/CuO(V_O)$. Thus, we focused on the C_2 coupling energy barrier. Generally, the C_2 coupling occurs as dimerization of two adsorbed CO species on the surface.
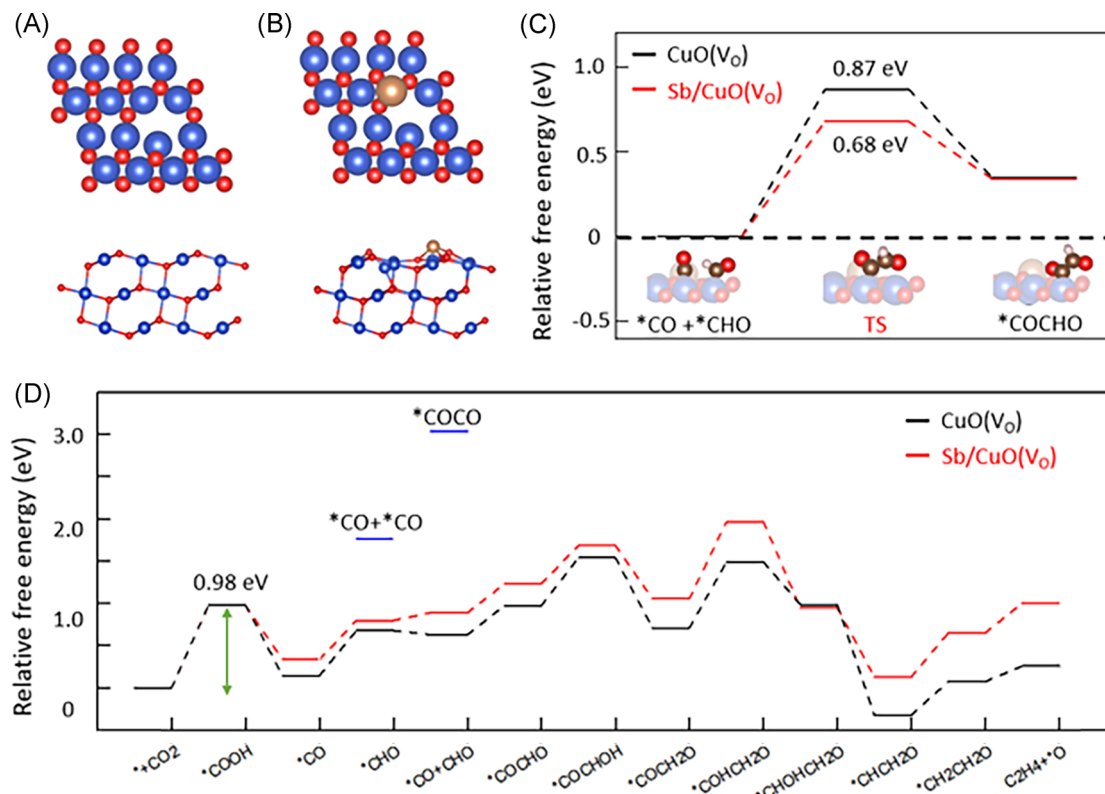
FIGURE 6 Top view and side view of (A) $CuO(V_O)$ and (B) $Sb/CuO(V_O)$. Blue, brown, red, black, and white spheres represent Cu, Sb, O, C, and H atoms, respectively. (C) C_2 coupling (*CO + *CHO → *COCHO) energy barrier on CuO(VO) (black), and Sb/CuO(VO) (red) models. (D) Free energy diagrams for CO_2 to C_2H_4 on $CuO(V_O)$ (black), $Sb/CuO(V_O)$ (red), and for COCO coupling on $Sb/CuO(V_O)$ (blue)

However, according to the energy diagram (Figure 6D), the relative free energy of *COCO (3.04 eV) on $Sb/CuO(V_O)$ was 2.15 eV higher than that of *COCHO (0.89 eV) on $Sb/CuO(V_O)$. Therefore, we considered the CO–CHO coupling. The *CO and *CHO are coupled to form *COCHO, which is a suggested C_2 coupling pathway on Cu surface.[30] As shown in Figure 6C, the $Sb/CuO(V_O)$ exhibits a lower activation barrier (0.68 eV) than $CuO(V_O)$ (0.87 eV) by 0.19 eV, indicating a facile C_2 coupling on the Sb modified surface. We also note that the activation energy of C_2 coupling for $Sb/CuO(V_O)$ (0.68 eV) is lower than 0.75 eV, a typical activation barrier corresponding to experimental TOF of $1s^{-1}$ at room temperature.[31] These results agree well with the higher C_2H_4 FE on $Sb/CuO(V_O)$ than that on $CuO(V_O)$ in the experiment (Figure 4B). As a consequence, a low C_2 coupling barrier (0.68 eV) on $Sb/CuO(V_O)$ compared to $CuO(V_O)$ seems to be the origin of the improved C_2 production and selectivity of the $Sb/CuO(V_O)$. These results validate that the $Sb/CuO(V_O)$ cascade catalyst can promote the C_2 coupling and improve the C_2 selectivity of CO_2 reduction reactions.

3 | CONCLUSION

We have demonstrated remarkably enhanced selective electrochemical CO_2 conversion to C_2H_4 at low overpotentials by jointly incorporation of single Sb atoms and defects in CuO. The ECR performance can be fine-tuned by adjusting the contents of Sb and oxygen vacancies as well as the electrolyte type. A particularly high reduction current density toward C_{2+} products approaching 12 mA/cm² is attained at −1.1 V in 0.1 mol/L CsBr solution with an H-type cell. The ECR performance retains good stability with an essentially constant C_2H_4 FE even after continuous polarization over 16 h. Especially, the as-made $Sb/CuO(V_O)$ delivers an overall ECR FE of 89.3% and a C_2H_4 FE of 58.4% with a current density of 500 mA/cm² in a flow reactor. DFT calculations in combination with in situ XRD showed that the Sb sites and oxygen vacancies synergistically lower the C–C coupling barriers to a great extent, thereby facilitating C_2H_4 formation. This study offers new insights into the design and synthesis of advanced electrocatalysts for efficient CO_2 electrolysis.

CONFLICTS OF INTEREST
The authors declare no conflicts of interest.

ORCID
Zhenyu Sun 🄳 http://orcid.org/0000-0001-5788-9339

## REFERENCES

1. Centi G. Smart catalytic materials for energy transition. *SmartMat*. 2020;1(1):e1005.
2. Wang N, Miao RK, Lee G, et al. Suppressing the liquid product crossover in electrochemical CO_2 reduction. *SmartMat*. 2021; 2(1):12-16.
3. García de Arquer FP, Dinh C-T, Ozden A, et al. CO_2 electrolysis to multicarbon products at activities greater than $1\ A\ cm^{-2}$. *Science*. 2020;367(6478):661-666.
4. Li F, Gu GH, Choi C, et al. Highly stable two-dimensional bismuth metal-organic frameworks for efficient electrochemical reduction of CO_2. *Appl Catal B Environ*. 2020;277: 119241.
5. Huang JE, Li F, Ozden A, et al. CO_2 electrolysis to multicarbon products in strong acid. *Science*. 2021;372(6): 1074-1078.
6. Hao L, Sun Z. Metal oxide-based materials for electrochemical CO_2 reduction. *Acta Phys—Chim Sin*. 2021;37: 2009033.
7. Zhu L, Lin Y, Liu K, et al. Tuning the intermediate reaction barriers by a CuPd catalyst to improve the selectivity of CO_2 electroreduction to C_2 products. *Chin J Catal*. 2021;42(9): 1500-1508.
8. Yang C, Nosheen F, Zhang ZC. Recent progress in structural modulation of metal nanomaterials for electrocatalytic CO_2 reduction. *Rare Met*. 2021;40(6):1412-1430.
9. Han BX. Phase engineering of metal nanomaterials for high-performance electrochemical CO_2 reduction. *Acta Phys-Chim Sin*. 2021;37(7):2012011.
10. Zhao Z, Park J, Choi C, et al. Engineering vacancy and hydrophobicity of two-dimensional $TaTe_2$ for efficient and stableelectrocatalytic N_2 reduction. *Innovation*. 2022;3(1): 100190.
11. Fan Q, Zhang M, Jia M, Liu S, Qiu J, Sun Z. Electrochemical CO_2 reduction to C_{2+} species: heterogeneous electrocatalysts, reaction pathways, and optimization strategies. *Mater Today Energy*. 2018;10:280-301.
12. Nitopi S, Bertheussen E, Scott SB, et al. Progress and perspectives of electrochemical CO_2 reduction on copper in aqueous electrolyte. *Chem Rev*. 2019;119(12): 7610-7672.
13. Jiang Y, Choi C, Hong S, et al. Enhanced electrochemical CO_2 reduction to ethylene over CuO by synergistically tuning oxygen vacancies and metal doping. *Cell Rep Phys Sci*. 2021; 2(3):100356.
14. Song Y, Junqueira JRC, Sikdar N, et al. B-Cu-Zn gas diffusion electrodes for CO_2 electroreduction to C_{2+} products at high current densities. *Angew Chem Int Ed*. 2021;60(16):9135-9141.
15. Li YC, Wang Z, Yuan T, et al. Binding site diversity promotes CO_2 electroreduction to ethanol. *J Am Chem Soc*. 2019; 141(21):8584-8591.
16. Wu BH, Chung JY, Hung LY, Cheng MC, Peng SM, Chen IC. Facet-dependent active sites of a single Cu_2O particle photocatalyst for CO_2 reduction to methanol. *Nat Energy*. 2019;4(11):957-968.
17. Chu S, Li X, Robertson AW, Sun Z. Electrocatalytic CO_2 reduction to ethylene over CeO_2-supported Cu nanoparticles: effect of exposed facets of CeO_2. *Acta Phys Chim Sin*. 2021; 37(5):2009023.
18. Chu S, Yan X, Choi C, et al. Stabilization of Cu^+ by tuning a $CuO-CeO_2$ interface for selective electrochemical CO_2 reduction to ethylene. *Green Chem*. 2020;22(19):6540-6546.
19. Gao L, Qin D, Chen Z, Wu S, Tang S, Wang P. Ethylene selectivity in electrocatalytic CO_2 reduction on Cu nanomaterials: a crystal phase-dependent study. *J Am Chem Soc*. 2020; 42(29):12760-12766.
20. Wang L, Li X, Hao L, et al. Integration of ultrafine CuO nanoparticles with two-dimensional MOFs for enhanced electrochemical CO_2 reduction to ethylene. *Chin J Catal*. 2022;43(4):1049-1057. doi:10.1016/S1872-2067(21)63947-5
21. Kumar P, Mathpal MC, Prakash J, Viljoen BC, Roos WD, Swart HC. Band gap tailoring of cauliflower-shaped CuO nanostructures by Zn doping for antibacterial applications. *J Alloys Compd*. 2020;832:154968.
22. Lei Q, Zhu H, Song K, et al. Investigating the origin of enhanced C_{2+} selectivity in oxide-/hydroxide-derived copper electrodes during CO_2 electroreduction. *J Am Chem Soc*. 2020; 142(9):4213-4222.
23. Zhao Z, Choi C, Hong S, et al. Surface-engineered oxidized two-dimensional Sb for efficient visible light-driven N_2 fixation. *Nano Energy*. 2020;78:105368.
24. Geng Z, Kong X, Chen W, et al. Oxygen vacancies in ZnO nanosheets enhance CO_2 electrochemical reduction to CO. *Angew Chem Int Ed*. 2018;57(21):6054-6059.
25. Wang W, Zhou Q, Fei X, et al. Synthesis of CuO nano- and micro-structures and their Raman spectroscopic studies. *CrystEngComm*. 2010;12(7):2232-2237.
26. Chen W, Liu X, Han B, Liang S, Deng H, Lin Z. Boosted photoreduction of diluted CO_2 through oxygen vacancy engineering in NiO nanoplatelets. *Nano Res*. 2021;14(3): 730-737.
27. Sing KSW. Reporting physosorption data for gas/solid systems. *Pure Appl Chem*. 1985;57(11):603-619.
28. Guo W, Liu S, Tan X, et al. Highly efficient CO_2 electroreduction to methanol through atomically dispersed Sn coupled with defective CuO catalysts. *Angew Chem Int Ed*. 2021;60(40): 21979-21987.
29. Peterson AA, Abild-Pedersen F, Studt F, Rossmeisl J, Nørskov JK. How copper catalyzes the electroreduction of carbon dioxide into hydrocarbon fuels. *Energy Environ Sci*. 2010;3(9):1311-1315.

30. Garza AJ, Bell AT, Head-Gordon M. Mechanism of CO_2 reduction at copper surfaces: pathways to C_2 products. *ACS Catal.* 2018;8(2):1490-1499.

31. Nørskov JK, Studt F, Abild-Pedersen F, Bligaard T. *Fundamental concepts in heterogeneous catalysis.* John Wiley & Sons; 2014:105.

AUTHOR BIOGRAPHY
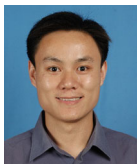
Zhenyu Sun completed his PhD at the Institute of Chemistry Chinese Academy of Sciences in 2006. He carried out postdoctoral research at Trinity College Dublin (Ireland, 2006–2008), Ruhr University, Bochum (Germany, 2011–2014), and the University of Oxford (UK, 2014–2015). He is currently a full professor at the College of Chemical Engineering at Beijing University of Chemical Technology (China). He was awarded a Humboldt Research Fellowship for Experienced Researchers (Germany). His current research mainly focuses on energy conversion reactions.

SUPPORTING INFORMATION

Additional supporting information can be found online in the Supporting Information section at the end of this article.